Journal Pre-proof

3D printed catalytic reactors for aerobic selective oxidation of benzyl alcohol into benzaldehyde in continuous multiphase flow

Clement Jacquot, Vesna Middelkoop, Angela Köckritz, Andrej Pohar, Regina Bienert, Suela Kellici, Ioan-Alexandru Bărăgău, Baldassarre Venezia, Asterios Gavriilidis, Blaz Likozar, Andrew M. Beale

Please cite this article as: C. Jacquot, V. Middelkoop, A. Köckritz, et al., 3D printed catalytic reactors for aerobic selective oxidation of benzyl alcohol into benzaldehyde in continuous multiphase flow, *Sustainable Materials and Technologies* (2021), https://doi.org/10.1016/j.susmat.2021.e00329

This is a PDF file of an article that has undergone enhancements after acceptance, such as the addition of a cover page and metadata, and formatting for readability, but it is not yet the definitive version of record. This version will undergo additional copyediting, typesetting and review before it is published in its final form, but we are providing this version to give early visibility of the article. Please note that, during the production process, errors may be discovered which could affect the content, and all legal disclaimers that apply to the journal pertain.

3D printed catalytic reactors for aerobic selective oxidation of benzyl alcohol into benzaldehyde in continuous multiphase flow

Clement Jacquot[a,b*], Vesna Middelkoop[b*], Angela Köckritz[c], Andrej Pohar[f], Regina Bienert[c], Suela Kellici[e], Ioan-Alexandru Bărăgău[e], Baldassarre Venezia[d], Asterios Gavriilidis[d], Blaz Likozar[f], Andrew M. Beale[a,g]

[a] Department of Chemistry, University College London, 20 Gordon St, London WC1H 0AJ, United Kingdom

[b] Sustainable Materials Management, Flemish Institute for Technological Research, VITO, Boeretang 200, 2400 Mol, Belgium

[c] Leibniz-Institut für Katalyse, LIKAT, Albert-Einstein-Straße 29A, 18059 Rostock, Germany

[d] Department of Chemical Engineering, University College London, Torrington Place, London WC1E 7JE, United Kingdom

[e] School of Engineering, London South Bank University, 103 Borough Rd, London SE1 0AA, United Kingdom

[f] National Institute of Chemistry, Hajdrihova 19, PO Box 660, SI-1001 Ljubljana, Slovenia

[g] Research Complex at Harwell, Rutherford Appleton Laboratory, Harwell Oxford, Didcot OX11 0FA, United Kingdom

*corresponding authors: clement.jacquot.17@ucl.ac.uk; vesna.middelkoop@vito.be; andrew.beale@ucl.ac.uk

Abstract

In this work, novel, patterned monolithic reactors were devised to explore more efficient routes for reactant conversion in order to investigate their potential to replace the packed bed and batch reactors conventionally employed in chemical industries. Well-defined bimetallic formulations were developed to substitute platinum group metals and critical raw materials such as palladium and cobalt, at least in part, by less active, but more sustainable and cost-effective metals such as earth-abundant iron. FePd and FeCo based monoliths were 3D printed and stacked in a continuous flow tubular reactor for testing the selective oxidation of benzyl alcohol (BA) into benzaldehyde (BZ) under mild conditions (80-100 °C and atmospheric pressure). The novel monolithic reactors were evaluated against current state-of-the-art reactor technologies, conventional packed bed and batch reactors. The FeCo- and FePd-Al2O3-supported monolithic catalyst beds showed higher conversion and TOF than their packed bed counterparts under the same operating conditions, revealing the impact of the novel design on both regular geometry and composition. What is of particular interest in the catalytic measurements shown is that the combined stacking of two monoliths in a flow reactor, Al_2O_3-supported Fe and GO-supported FePd catalysts, can significantly improve the performance with an increase in TOF of up to 90% in comparison to their FePd analogues. Mathematical modelling was used to obtain additional insights into the physical

and chemical processes governing the rate of BA conversion. It was found that due to the flow regime inside the microchannels, an axial dispersion model was appropriate, which allowed for mapping the concentration profiles of the reactants and products within the respective monolith geometries.

Keywords: Continuous flow reactor · Heterogeneous Catalysis · 3D printed catalysts · Benzyl alcohol oxidation · Alcohol aerobic oxidation

1. INTRODUCTION

Over the past 10 years, the organic chemical industry has shown a growing interest in the development of continuous systems for gas- and liquid-phase reactions, where the catalyst is retained within a fixed bed (rather than having to be removed from the product stream). [1,2] More recently, there has been a gradual switchover from conventional stirred batch reactors to plug flow reactors, in particular for the production of fine chemicals and pharmaceuticals. The emerging (continuous) flow reactor technology offers clear advantages in terms of greater control of operating parameters (that can be varied on the fly) such as reagent concentration, temperature, pressures, usage of volume with the benefits of high surface-area-to-volume ratios, changes in reaction kinetics, product ratios and their yield. The latter can ensure better surface contact between the phases and reduce mass and heat transfer limitations. The modular nature and design flexibility of the multi-channel continuous flow reactors allow for ease of scalability and integrated operation, safety advantages and more (atom) economical organic synthesis[3,4].

The oxidation of alcohols to aldehydes and ketones is crucial from an industrial point of view because compounds containing carbonyl groups are intermediates of various valuable speciality chemicals such as fragrances, flavourings, perfumes, flame retardants and pharmaceuticals[5]. The oxidation of alcohol is of relevance to the fine chemicals industry, particularly the oxidation of primary alcohols to aldehydes in the synthesis of valuable intermediates. Among these intermediates, benzaldehyde is one of the most produced molecules in synthesis processes involving the oxidation of alcohols, due to the rising demand for its derivatives [6,7]. To evaluate the efficiency of the new catalyst design, benzyl alcohol oxidation to benzaldehyde was used as a model reaction [8–10]; a well-referenced reaction for iron, cobalt and palladium-based catalysts[8–16]. Significant advances have been made in applying various metals and supports to the selective oxidation of benzyl alcohol, mostly in batch systems and less commonly in lab-scale flow reactor systems[17,18]. This involves the use of metal promoters such as ruthenium[18–20], platinum[17,21], rhodium[22], copper[23], chromium[24], bimetallic gold-palladium and gold catalyst[15,21–24]. Furthermore, in order to develop a process with greener credentials, we used molecular oxygen in combination with an aqueous solvent[11,25–27].

3D printing technology for catalyst fabrication and chemical synthesis is in the early stages of development. However, 3D printed, and micro-structured monoliths hold considerable promise for delivering more performant solutions in reactor design[28–

[30]. 3D printed monoliths offer several advantages over their conventional counterparts of random packings of pellets, such as high surface-area-to-volume ratio, low-pressure drop along the reactor and improved mass and heat transfer. Previously, 3D micro-structured reactors were applied in catalytic continuous flow processes in the gaseous phase and batch multiphase reactors, taking advantage of the newly developed formulations with tailor-made geometries[31–34]. Most recently, two different types of 3D printed ceramic structures, impregnated with 2 wt% Pd structures, were investigated in flow reactors for the hydrogenation of squalene into squalane, showing excellent conversion rates at temperatures from 180°C to 240°C, at a pressure of 25–30 bar.[35] To date, there has been some notable research on selective oxidation of benzyl alcohol (BA) to benzaldehyde (BZ), such as TiO_2[36] or ZnO-coated[37] continuous flow photocatalytic micro-reactors (∼ 100-500µm), as well as research on Pt coated extruded carbon monoliths with a channel size of 3 mm × 3 mm[17]. In the present work, a series of novel and well-tuned formulations of iron, cobalt and palladium, deposited onto γ-Al_2O_3 or graphene oxide (FeCo@Al_2O_3, FePd@Al_2O_3 and FePd@GO), have been 3D printed into monoliths with a 600-800µm channel size. The monoliths were integrated into a flow reactor for triphasic (gas-liquid-and solid) selective oxidation from BA to BZ under mild operating conditions (80-100 °C and atmospheric pressure). The potential of 3D printed monoliths in BA oxidation was evaluated to establish whether the palladium content could be reduced or completely replaced by iron or cobalt, in order to gain improved catalytic performance compared to the current processes. In addition, the impact of both regular geometry and composition was demonstrated by comparing monolithic catalyst beds to their packed bed counterparts under the same operating conditions and to their analogues under batch reactor conditions.

To obtain further insight into the benzyl alcohol oxidation reaction to benzaldehyde, modelling of the reaction has been performed to evaluate the effect of the operating conditions and map the concentration profiles. The mass balances inside the monolith reactor were calculated by considering convective transport with axial dispersion and chemical reaction in the liquid phase as well as oxygen transport from the gas to the liquid phase. The axial dispersion coefficient was determined, as well as the reaction kinetics, by regression analysis with the obtained experimental data.

2. MATERIALS AND METHODS
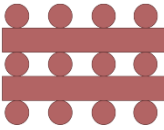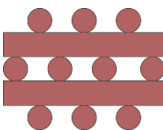
2.1 Catalyst Preparation

Alumina supported catalysts have been synthesised using a wet co-impregnation method similar to the one documented in the literature for iron[39], cobalt[40] and palladium[41] precursors. The bimetallic catalysts were prepared with three salts, purchased from Sigma Aldrich: $Fe(NO_3)_3.9H_2O(s)$, $Co(NO_3)_2.6H_2O(s)$ and $Pd(NO_3)_2.4NH_3$. They were dissolved in water to the desired concentrations aiming at 15 wt.% Fe, 15 wt.% Co and 1 wt.% Pd; see an overview of the obtained compositions in Table 1.

Puralox TH 100/150 Alumina powder, obtained from Sasol, was stirred for 24 h with the appropriate amount of catalyst precursors. The resulting precipitate was collected and dried for 24 - 48h in an oven at 80 °C. An additional bimetallic 15wt.% Fe-1wt.% Pd was deposited on graphene oxide support powder by utilising an environmentally benign, single-step and rapid chemical synthesis route, Continuous Hydrothermal Flow Synthesis (CHFS), as previously described.[31] Prior to the printing process, the catalyst powders were crushed and sieved through a 45μm mesh to ensure good flowability and smooth extrusion through the nozzle.

The inks (pastes) for the extrusion-based 3D printing (direct write) were mixed to obtain the desired and reproducible rheological properties. The formulation of the printing paste was based on methylcellulose, a typical polymer binder, which, after being removed by thermal decomposition, left the resulting structure behind with 80 wt.% dry solid content of the supported catalytic material and 20wt% bentonite additive. The printing process involved optimising the printing parameters for the ink to exit through 600 and 800 μm diameter nozzles and stack layers in three selected patterns (see Table 1 and Table S1).

After printing, the monoliths were dried in a humidity chamber at 25 °C for two days to remove excess moisture from the binder and give the structure its firmness. Prior to catalytic testing, the dry monoliths were subjected to thermal treatment at a slow heating rate of 1°C min^{-1} to 500 °C under 100 mL min^{-1} He to remove the organic binder from the printed catalyst bodies. Subsequently, once 500 °C was reached, the monoliths were activated under 20% O_2 in He for 2 hours. After that the catalysts were flushed with 100 % He for 30 min and then reduced in 50% H_2 in He for 4h, at 500 °C with a total flow rate of 100 mL min^{-1} to reduce metal oxides to their respective metallic forms.

Table 1. 3D Printing of Fe-containing supported monolithic catalysts using the micro-extrusion-based direct-write 3D technique: (top row) two geometries studied; (middle row) a close-up of CAD model unit cells; (bottom) examples of monoliths printed in different dimensions and compositions with fibre diameters and interfibre distances of 800 μm and 600 μm; the neighbouring channels are connected

Lattice type (cross section)	'1-1' straight channels	'1-3' crossed channels
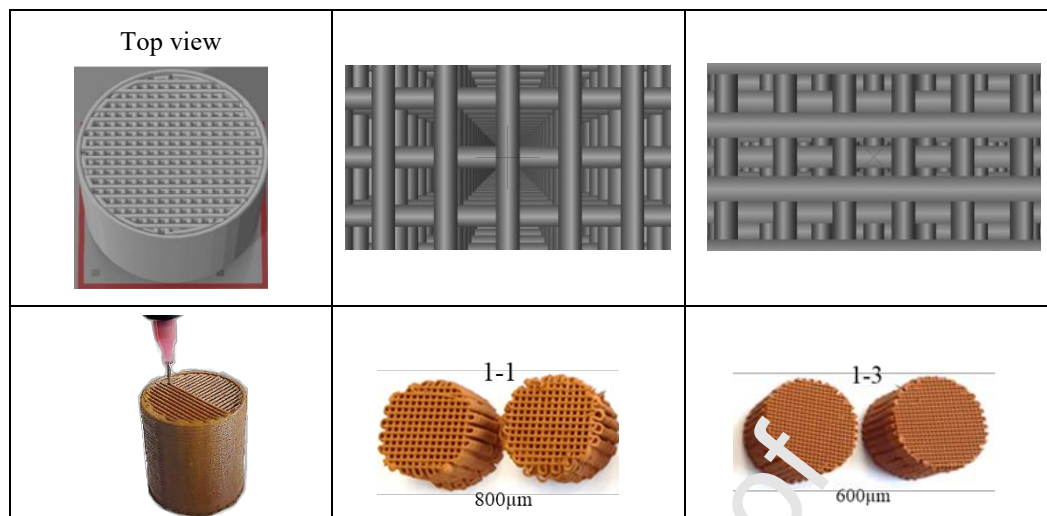
2.2 Reactor set-up and catalyst testing

The screening of 3D printed catalytic monoliths was carried out in a set up with a tubular reactor under continuous flow. Figure 1 presents a schematic of the set-up. The monoliths as well as packed bed samples, were mounted into a stainless-steel column reactor. Both the batch and packed bed samples were crushed monoliths sieved to fractions representative of monolith fibres within a range of 800±20 µm. 3D printed monoliths or their pellet analogues were loaded from the top of the reactor tube and placed between an inert packing media of quartz sand – grain size between 780µm-820µm. In addition, quartz wool was placed at the top and bottom of the catalyst bed. The quartz sand and quartz wool placed on the top of the catalyst bed were expected to promote pre-mixing and ensure an equal liquid flow distribution before reaching the bed of catalysts. The volume of the reactor taken up by two catalyst monoliths was estimated to be around 16 cm³, with a 21.6 mm diameter and 48 mm total catalyst bed height. The retention time of the feed mixture depended on the liquid flow. The gas and liquid flows were fed to the reactor column co-currently from the top. Under gravitational influence, the gas flow and liquid solution moved down the column through the catalyst bed.

A number of parameters were initially tested to identify the optimal set of operating conditions (see an overview of these preliminary parameters in the Supplementary Material, Tables S2 and S3). A HPLC Gilson 305 pump, fitted with a 10 mL pump head, provided a flow within a range of 0.01 to 10 mL.min^{-1}. The gas flow was varied between 1 to 100 mL.min^{-1}. After the initial parameters were set, the following conditions were selected to evaluate the 3D printed monoliths: a liquid flow of 0.1 mL.min^{-1} of 0.2 mol.L^{-1} BA (Benzyl Alcohol, purchased from Sigma Aldrich 99-100.5% GC) in dimethylformamide (DMF, purchased from Sigma Aldrich 99% solution) under a controlled synthetic air flow (purchased from Air liquid 99.5%) of 85 mL.min^{-1}, corresponding to 0.2086 mol/h, of which oxygen constitutes 21 %, which is 0.04381 mol/h. The reaction took place at

a temperature of 100 °C and 1 atm. DMF was both used as a solvent in the presence of K_2CO_3 (Potassium Carbonate Anhydrous,99.5%, VWR), saturated up to a maximum of 30 mg.L^{-1}, and as a base preventing the oxidation of benzaldehyde to undesired benzoic acid. In addition, oxygen was dissolved in a saturated amount in DMF. DMF has been selected as the most suitable solvent due to its boiling point of 145 °C and the favourably high solubility of the organic reactant within it.

The experiments in the flow reactor were carried out with a set of parameters chosen to achieve a flowing steady-state and maximum retention time for a duration of 4h. After 4h, the product samples were collected at the bottom of the column once an hour for another 4 hours. Under batch conditions 50 mg of catalyst pellets prepared from the crushed monoliths was placed in a 70 mL stainless steel autoclave and stirred for 8h at 100°C under 5 bar of air in the presence of 0.2 mol.L-1 benzyl alcohol and 50 mL of the DMF solvent saturated in the K_2CO_3 salt in an identical manner as that for the continuous flow experiment. The concentration of the reaction product in the mixtures was analysed by High Performance Liquid Chromatography (HPLC) using a Thermo Scientific Dionex UltiMate 3000 instrument.

The following equations have been used to derive reaction parameters and calculate conversion, selectivity and Turn Over Frequency (TOF):

A. Molar Flow benzyl Alcohol

Unit: $[mol]_{BA} \cdot [L]^{-1} \cdot [min]^{-1}$

$$\dot{F}^{in}_{BA} = [BA] \times \dot{Q}^{tot}_{liquid}$$

B. Conversion benzyl Alcohol

Unit: [standard] or [%]

$$X^{out}_{BA} = 1 - \frac{\dot{F}^{out}_{BA}}{\dot{F}^{in}_{BA}}$$

C. Productivity of catalyst

Unit: $[mol]_{BA\ converted} \cdot [min]^{-1} \cdot [g]^{-1}_{cat\ metal}$

$$p_{BA} = \frac{\dot{F}^{in}_{BA} \times X^{out}_{BA}}{m^{tot}_{cat\ metal}}$$

D. TOF

Unit: $[mol]_{BA\ converted} \cdot [min]^{-1} \cdot [mol]^{-1}_{cat\ metal}$

$$TOF = p_{BA} \times \hat{M}_{cat\ metal}$$

E. [$\hat{M}$]

Average molar mass catalytic sites per quantity of catalyst

Unit: $[g] \cdot [mol]^{-1}_{cat\ metal}$

$$\hat{M}_{cat\ metal} == \frac{\left\{\sum_i M_{cat\ metal_i} \times m_{cat\ metal\ i}\right\}}{m_{monoliths}}$$

F. Selectivity into Benzaldehyde

Unit: [standard] or [%]

$$S_{BZ}^{out} = \frac{\dot{F}_{BZ}^{out}}{\dot{F}_{BA}^{in} \times X_{BA}^{out}}$$

G. Retention Time on liquid flow

Unit: [min]

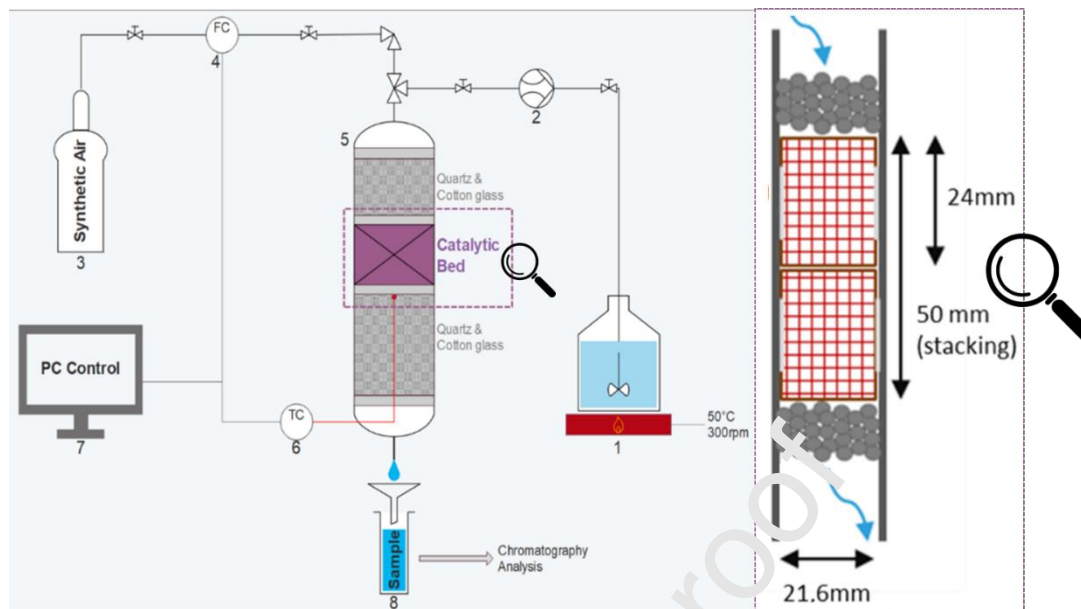$$\tau_{liquid} = \frac{V_{monolith\ section}}{Q_{liquid}^{out}}$$

Figure 1. Left: schematic diagram of continuous flow tubular reactor showing (1) liquid solution on a VWR® stirrer-hot plate; (2) Gilson® 305 HPLC pump; (3) synthetic air, $O_2:N_2/21:78$; (4) Brooks® mass flow controller; (5) stainless steel column fed from the top containing the catalyst bed between layers of quartz; the steel column was placed in a Carbolite® high-temperature furnace; (6) thermocouple inserted from the bottom and connected to software for real-time data logging (7) computer control for reactant flow and temperature monitoring; (8) reactor-outlet for product sampling via the HPLC pump. Right: schematic illustration of the monolith stack in the reactor (this image is not scaled to size).

The RTD (Residence Time Distribution) measurements were performed for both the monoliths and their packed bed analogues in the same set-up except for using a Harvard Apparatus PHD ULTRA syringe pump to supply the diode I_2 salt solution to the column and using a Mettler Toledo electrometer to measure conductivity. The solution samples were collected at the bottom of the column. After firstly passing deionised water as a non-conductive reference, the salt solution with a significant conductivity was introduced into the column. Subsequently, the conductivity of the solution samples was measured to determine which fraction was still deionised water or a salt solution and at which point it had turned into a pure salt solution.

Comparable catalytic reactions have been performed in batch conditions. In a stainless-steel autoclave reactor of 70 mL a DMF volume of 50 mL saturated in K_2CO_3 and 0.2 mol.L^{-1} BA was mechanically stirred for 8h under 5 bar of air at 100 °C in presence of 50 mg of catalytic material in powder form.

2.3 Catalyst characterisation

The surface area (Brunauer Emmett Teller, BET) and porosity analyses of the catalysts were performed using nitrogen adsorption on a Quantachrome Autosorb IQ gas sorption analyser. The element content was determined using an MP-AES Agilent 5100 ICP analyser. The paste viscosity measurements were performed using a HAAKE MARS rheometer in a plate-to-plate configuration with a rotational continuous ramp of $0.01 \ s^{-1} – 100 \ s^{-1}$ at 25°C. The macro and microstructure and elemental distribution images were obtained using a FEI Nova NanoSEM 450 operated at 20 kV and coupled with an EDX (Energy Dispersive X-Ray Spectroscopy) QUANTAX 200 system. X-ray diffraction (XRD) analysis was carried out on a Philips/Panalytical X'Pert Pro powder diffractometer with a CuKα radiation source operated at 40 keV and 40 mA. X-ray photoelectron spectroscopy (XPS) measurements were carried out to determine the surface chemistry of the catalysts using a ThermoFisher Scientific ESCALAB 220iXL instrument.

2.4 Reactor modelling

The two-phase flow in the monolith reactor has a much higher gas than the liquid flow rate ($85 \ mL.min^{-1}$ gas to $0.1 \ mL.min^{-1}$ liquid at the inlet at 25 °C). Since the reaction takes place on the catalyst, it is presumed that DMF wets the walls and a DMF liquid film is formed on the monolith channels walls. A much higher gas flow rate is also present, which contributes to the liquid movement towards the reactor outlet through shear. Due to the irregular shape of the walls, namely the non-flat surfaces, the nonuniform thickness of the DMF film on the walls and nonuniform gas flow, the flow regime can be most closely approximated with a one-dimensional axial dispersion model for the liquid flow, which describes the level of axial mixing in comparison to the well-defined plug flow conditions.

The reactant and product concentration profiles inside the liquid phase of the fixed bed monolith reactor were calculated with an axial dispersion model considering the time, convection, dispersion and chemical reaction terms. Benzyl alcohol (BA) reacts with oxygen in the liquid phase on the catalytic walls, forming benzaldehyde and other by-products. Oxygen is involved in both reactions and is supplied from the gas phase (air) by mass transfer. The validity of the axial dispersion model was verified with residence time experiments. Because the liquid and gas phase are heated from 25 – 100 °C inside the reactor, Aspen Plus (AspenTech) calculations were used to determine the phase distribution at elevated temperatures using the Peng–Robinson equations of state. See the Supplementary Material for further details on modelling (such as partial differential equations). Several models of benzyl oxidation kinetics have been developed in recent years based on catalysts[27,42], solvents[43] and oxidants[43]. In most cases, the activation energy of these models depends on the conditions created and remain constant while the order of the reaction is one over benzyalcohol[44].

The geometry data of the monolith required for the model (cross-sectional area and channel volume) was taken from the CAD (computer-aided design) model prepared in SolidWorks (Dassault Systèmes). The actual average linear velocity of the liquid phase was determined together with the axial dispersion coefficient from the measurements of the residence time distribution with regression analysis using the Nelder–Mead optimisation algorithm. In a similar way, he kinetic constants were estimated by analysis of the kinetic data for the reactions taking place on the FeCo@Al$_2$O$_3$ catalyst. The system of partial differential equations, describing the mass balances, was transformed into a set of ordinary differential equations, which were solved with the Runge–Kutta 45 solver in Python (see the Supplementary Material). 3D printed monoliths as well as their CAD model with a close-up of the channels are presented in Table 1. Two monoliths were positioned inside the continuous flow reactor stacked on top of each other, within the reactor with an inner diameter of 21.6 mm. The monolith fibres were of circular shape with a diameter of 0.7 mm. The channels of the monolith were approximately 0.67 mm apart at the narrowest points and 1.26 mm from the centre of the walls in horizontal direction.
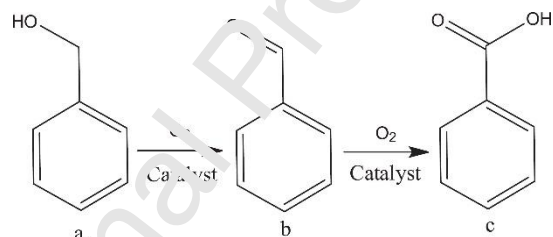

Figure 2. Schematic representation of (a) benzyl alcohol oxidation into (b) benzaldehyde and (c) possible by-product, benzoic acid

An inverse geometry was created for the computational fluid dynamics (CFD) simulations. Since the majority of the domain is comprised of repeating channels, only 1 channel was modelled. The effect of irregular channels at the monolith edge were not considered in this work, but large deviations from the rest of the monolith solution are unlikely. The velocity and pressure profiles were obtained for the incompressible laminar fluid flow with COMSOL Multiphysics. The inlet boundary condition was 6.76×10^{-3} m s^{-1}, while the channel walls had the no-slip boundary condition. Symmetry was prescribed at the surfaces where the channels are in contact with each other. At the outlet, zero pressure and zero velocity gradient were set. The mesh was composed of approximately 500k tetrahedral elements. Grid independence was checked with denser and coarser meshes.

3. RESULTS AND DISCUSSION

3.1 Physico-chemical characterisation of 3D printed monoliths

The formulation of the paste material constitutes a decisive step towards obtaining the desired characteristics of the final structures, including satisfactory mechanical stability which required an adequate calcination step. The aim was to avoid potential organic binder residual, structure shrinkage and fracture. The particle size of the starting powder components, rheological behaviour of the printing inks, as well as the pH of the mixtures (of ca. 5.0) were maintained in the optimal range to ensure composite flowability and a smooth printing process. The printing inks exhibit non-Newtonian, shear-thinning behaviour with the viscosity in the range of 500 to 5000 mPa·s (see Figure S2 in the Supplementary Material for typical viscosity versus shear rate curves). The typical particle size of the sieved powders used for ink mixing was ca. 30 μm (D90) for $FeCo@Al_2O_3$ and $Pd-Fe@Al_2O_3$ respectively.

The measured ICP values for metal loading, specific surface area, pore radius and volume of the samples are shown in Table 2. The molar ratio between iron Fe and co-metal stays constant for the duration of the calcination and reaction processes. The leaching of metals after the reaction is negligible due to the similar metal content measured in the fresh and spent catalysts. The elemental concentrations obtained by ICP are close to those of the (theoretical) target Fe, Co and Pd compositions.

Table 2. Overview of values for metal loading, surface area, porosity and pore diameter

Catalyst composition with nominal metal loading in wt%[a]	Actual molar ratio (Fe:M)	ICP (actual metal loading in wt%) [b]		BET Surface Area (m²/g)	Pore Volume (cm³/g)	Pore Diameter (nm)
		Fe	M			
Puralox[c] TH 100/150 Al_2O_3 powder	0	0	0	150	0.8-1.1	11
VWR Bentonite[c]	/	0	0	50	/	/
Printed Al_2O_3 calcined	0	0	0	165	0.68	11.8
FePd@Al_2O_3 as-synthesised powder	96.4 : 3.6	12.15	0.86	142	0.59	8.6
Printed FePd@Al_2O_3 calcined	96.8 : 3.2	8.84	0.56	85	0.30	8.6
Printed FePd@Al_2O_3 spent	96.9 : 3.1	8.89	0.55	75	0.22	8.6
FeCo@Al_2O_3 as-synthesised powder	47.9 : 52.1	11.54	13.23	129	0.54	8.0
Printed FeCo@Al2O3 calcined	44.9 : 55.1	8.51	11.03	103	0.49	19.1
Printed FeCo@Al2O3 spent	43.4 : 56.6	8.52	11.15	84	0.45	16.4
Abalonyx[c] Graphene Oxide powder	44.6 : 55.4	0	0	~1600	/	/
Printed FePd@GO calcined	96.9 : 3.1	13.45	0.71	223	/	/
Printed FePd@GO Spent	95.0 : 5.0	13.28	0.70	/	/	/

[a] Nominal catalytic material. Percentage calculated on basis of the support weight. Initial theoretical metal loading was calculated at wet impregnation step.

[b] Percentage calculated on basis of the final catalyst weight (determined by ICP).

More detailed data obtained from the nitrogen adsorption–desorption isotherms of the printed catalysts presented in Table 2 include the specific surface area using the BET method, pore size distribution and mesopore volumes derived from the desorption branch of isotherms using the Barrett-Joyner-Halenda (BJH) method. Both FeCo@Al$_2$O$_3$ and FePd@Al$_2$O$_3$ materials exhibit Type IV isotherms showing a hysteresis loop in the P/Po region of 0.4 -1.0 indicative of mesoporous materials (see Figure S3 in the Supplementary Material). The micropore volume and micropore surface area determined using the t-plot method showed that the micropores make a negligible contribution to the total specific surface area. It can be seen from the N$_2$ adsorption data for both catalyst materials that impregnation of the Al$_2$O$_3$ support and subsequent calcination led to a progressive reduction in the surface area as well as the pore volume. However, the calcined printed FeCo@Al$_2$O$_3$ catalyst had a higher surface area than that of its FePd analogue. Its pore diameter increased through the calcination step while it decreased slightly during the reaction. This could be attributed to particle sintering during the calcination step which can cause the blocking of some of the Al$_2$O$_3$ pores (the calcined Pd particles in particular are more likely to be larger than the uncalcined ones). The analysis after the reaction showed the BET surface area and pore volume decreased for both catalysts. It should be noted that these values decreased progressively over time due to a number of possible reasons, such as the accumulation of residual solid from the quartz sand filling of the reactor upstream of the catalytic bed and the local high concentration of K$_2$CO$_3$ solidifying and agglomerating into the available pores. The N$_2$ adsorption porosity results (pore radius and volume) are complemented by the SEM images of uniformly printed fibres and consistent cross-hatch patterns. The SEM images in Figure 3 and Figure 4 show

the macrostructure of the 3D printed monoliths as well as their highly porous microstructure with intra-fibre porosity and sufficiently high surface area tailored to host active catalytic species. The calcined structures shrunk to 85 % of the original size, which caused the initial inter-fibre spacing to be reduced. The change in the final external dimensions (i.e. volumetric shrinkage) of individual monoliths after the drying and calcination steps was assessed by measuring their diameter and height using a Vernier caliper and calculating the shrinkage results (of ca. 85%) as an average of 3-5 samples from the same printing batch. The actual fibre diameter and inter-fibre spacing with the nominal values of 800μm and 600μm were determined by taking measurements from the SEM micrographs.

The SEM and accompanying EDX images show different morphology of Fe-containing samples but uniform distribution of the active material in their micro-scale environment across the support and within the inorganic co-binder (bentonite) matrix. Blending the support materials (Al_2O_3 and GO) in the polymer matrix and its subsequent removal enables overall control over the particle dispersion. The EDX images in Figure 4 obtained at higher resolution confirm the uniform distribution of Pd particles across the GO-based support down to the sub-100 nm scale (in addition see a TEM image in Figure S10 in the Supplementary Material). In this study GO was introduced to be able to show the effect of different support morphologies due to the GO specific carbon atom network.
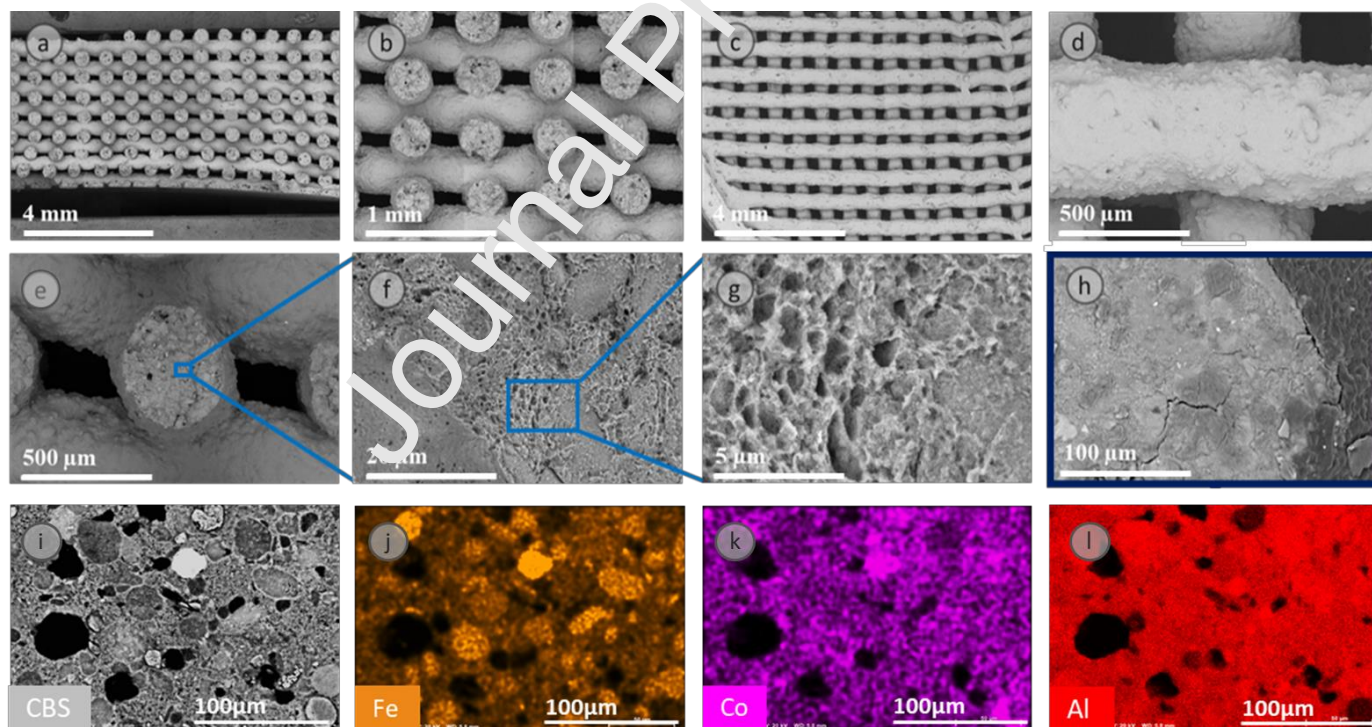

Figure 3 SEM images of 3D printed FeCo supported on Al_2O_3 monolith after calcination with straight channels of 600μm fibre thickness and 600μm spacing: a-b) SEM cross-section at two different magnifications; c-d) top-view of the structure; e-h) microstructure within the selected region of interest; i-l) EDX mapping of elements present corresponding to the region of interest within the fibre. (grey-CBS, orange-Iron, purple-Cobalt, red-Alumina at 100 μm scale bar)
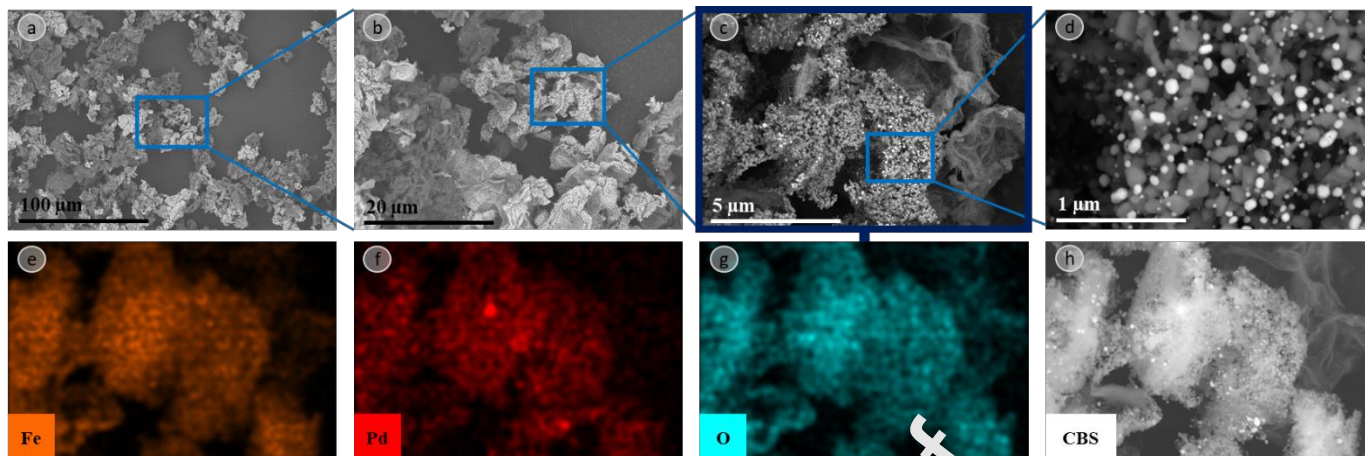
Figure 4. (Top row) SEM analysis of the morphology and particle dispersion of FePd on GO support; (bottom row) EDX elemental mapping of a selected region of interest showing Fe, Pd and O distribution (indicated by a blue square in c corresponding to the CBS image in h at 5μm scale bar).

Crystalline phases identified by XRD after heat-treatment before the reaction and after the reaction are presented in Figure S11). The XRD patterns confirm that the presence of metallic Fe is present in all the calcined and reduced samples prior to the reaction. The identification of the Fe species post reaction indicates Fe phase transformations during the reaction (in the presence of oxygen) and the formation of magnetite (Fe_3O_4) possibly due to the Fe(III) oxyhydroxide undergoing decomposition to Fe_2O_3 and high-temperature reduction. Probably worth adding a statement that Co and Pd phases are not seen in the sample by XRD since they are present at low concentration/signals obscured by the Fe phase(s) present.

The XPS survey spectra and individual peak profiles obtained for FeCo@Al$_2$O$_3$, FePd@Al$_2$O$_3$ and FePd@GO monoliths (shown in Figures S12-20) provide a more detailed information on the chemical state of the active catalyst species. A summary of the corresponding peak positions (binding energies) for each spent catalyst are given in Table S4 in the Supplementary Material.

A complementary set of XRD data and a high resolution XPS spectrum of the Fe2p orbital in FeCo@Al$_2$O$_3$ are presented in Figure 4 as well as in Figure S15 in the Supplementary Material. The sample exhibits mixed oxidation states indicating co-existence of CoO and Co$_3$O$_4$. This is in agreement with the XRD analysis (Figure 5 left). The Fe2p spectra for all the examined samples exhibit the co-existence of Fe in mixed oxide states (Fe$_2$O$_3$ and Fe$_3$O$_4$ species) which is in agreement with the XRD analysis (Figure S11).

Looking at the relative intensity of both Fe2p and Pd3d spectra it can be observed that FePd GO supported sample exhibits higher peak intensity and peak area than the Alumina supported sample indicating a significant difference in binding of the catalytic metal atoms on respective supports and their surface concentrations. XPS survey spectrum of FePd@GO exhibits the characteristic peaks for carbon (centred at 284.8 eV), oxygen (530.1 eV), Fe (710.4 eV) and Pd (337.1 eV). The XPS data corroborate the benefits of depositing particles onto the GO support: the GO support sample shows palladium in oxide state PdO, indicating the catalytic metal deposited binds preferentially on the free oxygen atoms of the support and, as a result, the FePd@GO monolith stacked onto a Fe@Al2O3 monolith was found to show a greater (up to 70% higher) selectivity towards BZ than two stacked FePd@Al$_2$O$_3$. In contrast the Al$_2$O$_3$ supported sample shows (two doublets of) palladium in its metallic state, Pd and ionic state Pd2+ and overlaps with Ca-2p in the 355-345eV region.
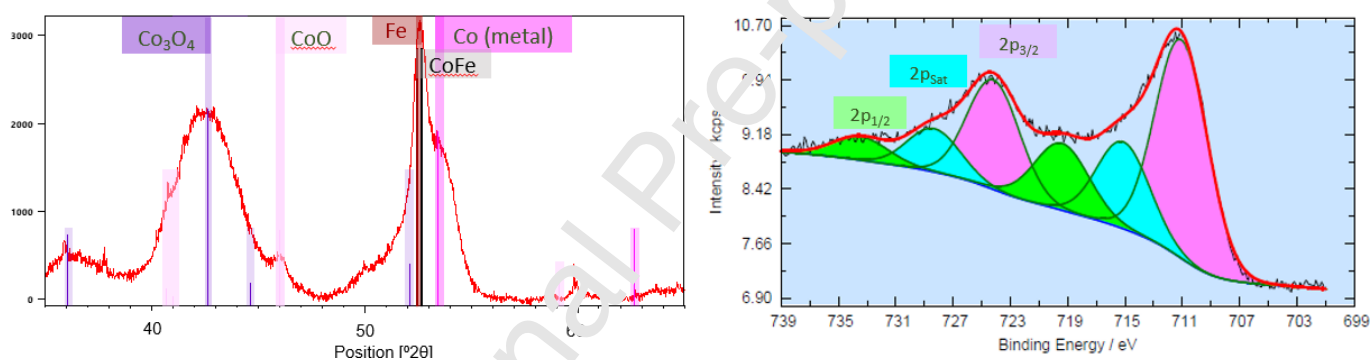

Figure 5. XRD and XPS complimentary analysis on representative FeCo@Al$_2$O$_3$ monolith and Co phases identified (after reaction).
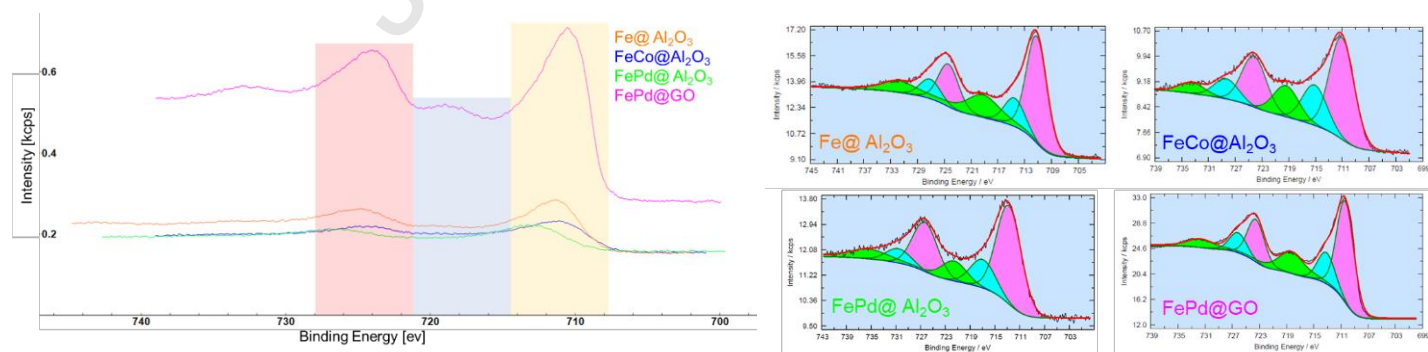

Figure 6 High resolution XPS Fe2p spectra for all four samples after reaction showing a characteristic peak with pronounced satellite features centred around a binding energy of 730 and 705eV

Figure 6 presents an XPS spectrum comparison of all Iron-containing formulations. The difference in the features of the Fe2p spectra is more pronounced for that of the FePd@GO spectrum in comparison to the Al_2O_3 supported compositions (further details are shown in Figure S14 in the Supplementary Material).

The results of the pressure drop measurements (see Figures S1, to S4) were used to support the selection of the preferred patterns (with the straight channels '1-1' and crossed channels '1-3'), fibre diameters and inter-fibre distances for printing the monoliths. The permeability of the monoliths was confirmed by pressure drop measurements.

3.2 Catalytic testing and discussion

In comparison to the preliminary tests conducted in a batch reactor for 8h (Figure 7 see a set of bars on the left of both plots), the 3D printed monoliths in the flow reactor with the same loading of iron and palladium exhibited equally high catalytic activity with a conversion rate of over 80 %, a Turn Over Frequency (TOF) of 0.01 h with a residence time of the two-phase mixture through the catalyst beds of about 2h and the total reaction time of 8 h; see Figure S8 in the Supplementary Material for detailed measurements of the residence time distribution for different catalyst beds.

Furthermore, the FeCo@Al_2O_3 and FePd@Al_2O_3 monolithic catalyst beds showed higher conversion and TOF than their packed bed counterparts under the same operating conditions, revealing the impact of the novel design concerning both regular geometry and composition. The 3D printing of catalyst monoliths offers a better control of the reaction process as the monolith geometry and its channels provide a high surface area to volume ratio for the reactant mixture to come into contact with the solid.

However, the catalytic conversion of BA occurring along the entire length of the FePd@Al_2O_3 monoliths (with the highly active Pd phase) leads to lower selectivity into BZ than in the batch reactor. This can be explained by the number of the Pd active sites available, at high conversion; the reaction proceeds into a consecutive reaction BZ to benzoic acid. Replacing Pd by Co as an alternative catalytic material offers still high selectivity at lower cost and improved sustainability even with up to five times higher selectivity to BZ (see comparison between FeCo@Al_2O_3 and FePd@Al_2O_3 monoliths; for further comparison see Table S2 and Table S3 in the Supplementary Material). In particular in the case of the FeCo@Al_2O_3 1-3 structures, the selectivity towards BZ is significantly higher in comparison to that of their FePd@Al_2O_3 1-3 analogues, thus pointing to a consecutive (secondary) reaction in favour of benzoic acid. The FeCo@Al_2O_3 '1-3' monoliths gave 60% selectivity to BZ and 30% to benzoic acid. It has previously been shown by the authors that the substitution of PMG based catalysts by even with a small fraction of other metal, such as Fe, Co (of about 1.5wt%) already can affect the selectivity (of 19%) toward benzoic acid[45].

In contrast, the FePd@GO monolith stacked onto a Fe@Al$_2$O$_3$ monolith was found to show a greater (up to 70% higher) selectivity towards BZ than two stacked FePd@Al$_2$O$_3$. It is interesting to observe that the selectivity towards BZ for the FePd@GO-Fe@Al$_2$O$_3$ stacking arrangement remains high (87%) at 60º C. The best overall performance for the FePd@GO - FePd@Al$_2$O$_3$ stacking arrangement can be attributed largely to the presence of Graphene oxide as a support. Indeed, the metal atoms of Iron and Palladium once deposited on GO, are extremely active due to their high accessibility to reactant. The graphene oxide support offers a high surface area and flake morphology. Therefore, the frequency of catalysed reaction is maximised. While keeping the same volume and weight of catalytic bed constant, this stacking arrangement enables the optimisation and rationalisation of already highly active FePd@GO: benzyl alcohol oxidation and conversion has just started in the first monolith, Fe@Al2O3 and is significantly progressing to the second monolith, FePd@GO which is selectively converting nearly all remaining benzyl alcohol.

In addition, see Figure S1 in the Supplementary Materials for typical results of the benzoic acid product that has been identified, as well as an additional by-product. This compound can be attributed to a secondary reaction occurring and is likely to be associated with a double phenyl group linked by a nitrogen atom. As reported by a number of authors, alongside benzoic acid other secondary by-products are detected during the benzyl alcohol oxidation: dibenzyl ether and benzyl benzoate[1,42,46].

A data comparison between the monoliths with a fibre thickness/interfibre distance of 800µm and 600µm indicates that a change in the dimensions within this range has a limited effect (of ca. 3% difference) on the performance of the monolith as whole (see Figure S9 in the Supplementary Material). In terms of the reliability of the findings, the 3D printed catalysts were repeatedly tested under the same benzyl alcohol oxidation conditions to ensure the stability of the 3D monoliths and reproducibility of the tests. The standard deviation of the reproducibility of catalyst testing was calculated to be Σ(XBA)= 1.32%, Σ(SBZ)= 1.34% and Σ(TOF)= 2.21% (see Figure S21 in the Supplementary Materials).

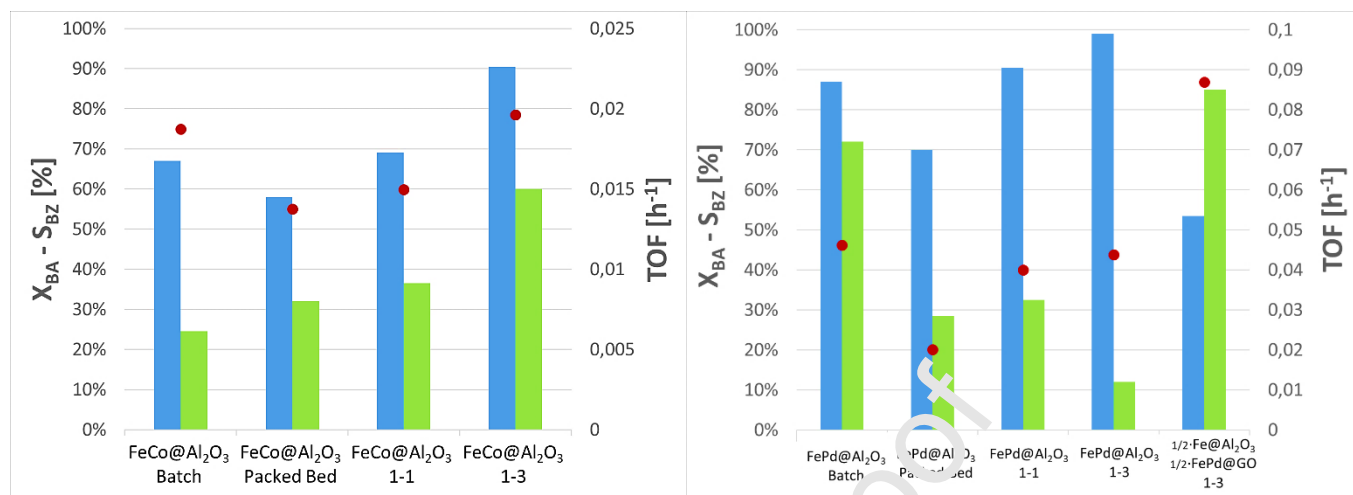The retention time measurements on the packed bed and monolith configurations are presented in Figure S10.

Figure 7 Performance comparison for 3D printed monoliths with their packed bed analogues for benzyl alcohol oxidation in continuous flow reactor as well as in batch reactor. Left: Fe and Co deposited on Al_2O_3; right: Fe and Pd deposited on Al_2O_3 and GO; reaction conditions in flow reactor: 100 °C, 1 atm, 1 mL.min⁻¹ of 0.2 mol.L-1 benzyl alcohol in DMF solution saturated in K2CO3 in co-current flow of air of 85 mL.min-1 passing through equal mass of catalytic material, 12 g of 3D printed catalyst monoliths with fibre thickness and interfibre distance of 800 μm or packed beds of crushed fractions of 3D printed monoliths sieved between 780 μm and 820 μm which is comparable to fibre diameters of monoliths. The reaction conditions in batch reactor: 0.2 mol.L-1 benzyl alcohol in 50 mL of DMF solvent saturated in K2CO3 in the presence of 50 mg of solid powder catalyst stirred for 8h at 100°C under 5 bar of air. Legend for both graphs: left bar corresponds to conversion of benzyl alcohol XBA(■) in %, right bar to selectivity into targeted benzaldehyde SBZ(■) in %; turn over frequency TOF (●) is expressed in h-1.

3.3 Modelling results and discussion

3.3.1 Flow characteristics

The major components in the case under consideration, air and DMF, are fed into the reactor with a molar flow ratio of 0.73:0.27 at a temperature of 100 °C. In this case, the calculated vapor fraction was 0.92 and the liquid fraction 0.08. Table S4a and Figure S6 show the phase equilibrium constitution for different temperatures at a DMF fraction of 0.27 and the values of the vapor fraction at different DMF fractions are shown in Table S4b. At 110 °C, it is expected that the whole mixture is in the gaseous phase. At 100 °C, if the DMF fraction is lower than around 0.2, the mixture as a whole is also in the gaseous phase. Table 3 shows the inlet reactant streams at 100 °C and 0.72 air fraction, which are the conditions used for the simulations.

Table 3. The inlet reactant streams at 100 °C and 0.72 air fraction.

Phase **Component Mole Flow**	Units	Vapour at 25 °C	Liquid at 25 °C	Vapour at 100 °C	Liquid at 100 °C
AIR	kmol h^{-1}	0.0002086	0	0.0002086	1.83×10^{-8}
DMF	kmol h^{-1}	0	7.74×10^{-5}	5.41×10^{-5}	2.34×10^{-5}
BA	kmol h^{-1}	0	1.16×10^{-7}	$3.?? \times 10^{-8}$	8.23×10^{-8}
Mole Flow	kmol h^{-1}	0.0002086	7.76×10^{-5}	0.0002627	2.35×10^{-5}
Mass Flow	kg h^{-1}	0.006039	0.005672	0.009993	0.001718
Volume Flow	L min^{-1}	0.085	0.0001	0.1336	3.29×10^{-5}
Temperature	°C	25	25	100	100
Pressure	bar	1.01325	1.01325	1.01325	1.01325
Vapor Fraction	[0/1]	1	0	1	0
Liquid Fraction	[0/1]	0	1	0	1

3.3.2 Reactor modelling

The molar fraction of O_2 in DMF at 25 °C is 3.89×10^{-4}.[47] One channel cross-section of the monolith is 1.44×10^{-6} m^2, while the volume of the channel is 3.59×10^{-8} m^3 (obtained from the 3D model). Firstly, the residence time distribution experiments were used to determine the liquid velocity (through the average residence time, without the reaction, Figure S9). The average residence time obtained was 82.5 min, while the axial dispersion coefficient was 5.37×10^{-8} m^2 s^{-1}. A good agreement of the fitted model and the results is presented in the breakthrough curve in Figure S7. Considerable deviation from plug flow behaviour can be observed and a wide residence time distribution (from approximately 25 – 150 minutes).

At 100 °C, the concentration of BA inside DMF entering the catalytic channel is 463.6 mol m^{-3}. 90.5 % conversion is achieved and selectivity toward benzaldehyde was 60 %. After regression analysis, the values for both kinetic constants for FeCo@Al$_2$O$_3$ catalyst were obtained: $k_{reak,1}' = 9.04 \times 10^{-8}$ m s^{-1} and $k_{reak,2}' = 6.80 \times 10^{-8}$ m s^{-1}. The concentrations of BA and BZ along the reactor length up until 250 min are presented in Figure S7. At that moment in time, steady-state is achieved, which can be seen

from the absence of further changes in the concentration in time. At $t = 0$ there is zero concentration of BA and BZ inside the channel. The outlet concentrations can be seen on the concentration profiles at x = 48 mm.
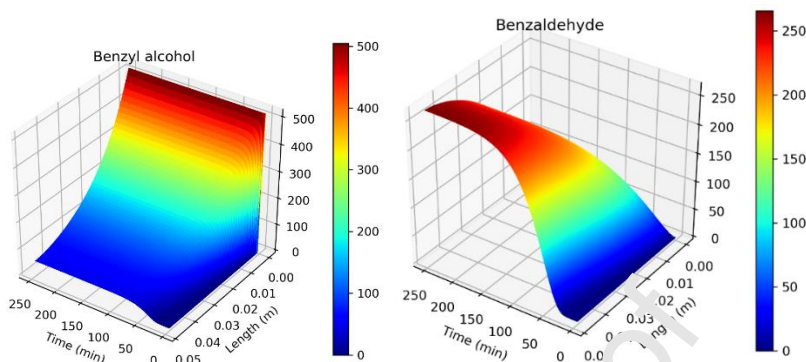

Figure 8. The concentration profiles of benzyl alcohol (left) and benzaldehyde (right) along the length of the reactor with time. The concentration is in mol m^{-3}.

The concentration profiles at 250 min at steady-state are presented in Figure S7. In the figure, the low saturated concentration of O_2 can be seen, which needs to be replenished by the flow of air. If mass transfer from the gas to liquid phase was not efficient, the amount of O_2 in DMF would be depleted, the concentration would be zero at all times and mass transfer of O_2 into DMF would be the limiting process. The experimental data present 90.5% BA conversion and 57% selectivity to BZ. The transient RTD measurements and the axial dispersion model provided a very good agreement and important insight into the reactor convection-dispersion dynamics, in this case showing a high level of dispersion in the system. Since the system is too complex for intrinsic kinetic studies and the identification of the precise chemical and physical background, it is only suitable and appropriate to provide a simple apparent kinetic model, which does not favour a particular mechanism, flow profile and mass transfer specifics, but it does consider the effect of the determined level of axial dispersion. Since the system is well mixed across the lateral cross-section, the obtained concentration profile should be very close to the actual one, which suffices for the basic requirement of the usefulness of a mathematical model and provides a visual representation of the conversion process.

3.3.2 Computational fluid dynamics

CFD simulations of mass transfer and chemical reactions can be accurately performed for both the liquid and vapor phase, also when the liquid and vapor phases are well defined in space. The majority of the fluid inside the microchannels is in vapor phase, while the liquid mostly flows along the channel walls and the CFD simulations were therefore performed for the vapor phase.

Figure 8 shows the fluid flow field and the pressure drop. A typical parabolic-type velocity profile, which is characterised by the highest velocity in the centre of the channel is formed. The velocity at the walls is zero. There are approximately 250 such channels in the monolith and this profile is assumed to be the same for each channel. It should be noted that the irregularly-shaped side channels have a more complex geometry (triangular or trapezoidal prisms). The flow in them has not been modelled separately as these channels have a smaller channel cross-section; hence a lower volumetric flow rate would be predicted at the same pressure drop conditions. For the kinetic model, however, all the effects of the irregular geometry were taken into consideration by the measured axial dispersion through the residence time distribution measurements. The solution is presented along the entire channel, showing, from left to right, the velocity field and the pressure field. The pressure drop is linear, as expected, and very small, mostly due to the low velocity.
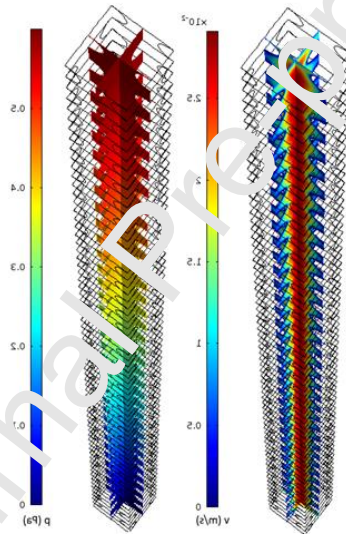

Figure 9. The velocity and the pressure fields along the entire length of the channel. The flow regime is not ideal and as such a model respecting the locations of both phases is not easily and objectively developed, and the 1D axial dispersion model offers a much better approximation of the actual reaction conditions inside the reactor. However, mostly gaseous flow is present inside the channels, and the much smaller amount of liquid is mostly located on the channel walls. In order to obtain the predominant gaseous velocity profile and its specifics, as well as the pressure drop of the system, the presented 3D model is the best approximation, and although it is not coupled with the reaction kinetics, it should give a good visualisation of the flow and pressure fields inside the channels, as can be expected in the reactor.

4. CONCLUSION

3D printed multi-channel catalytic reactors with tailored microporous bed architectures present a promising approach to improving continuous processes in terms of intensification, sustainability, and economic viability. 3D-microstructured reactors provide an attractive solution for multiphase heterogeneous catalysis such as selective oxidation of BA to BZ, making them a highly effective alternative to batch systems and PGM systems. The present work demonstrates the integration of different 3D printed catalyst configurations into a continuous process while allowing for optimal metal utilisation and significant reduction of the palladium content by iron or cobalt to gain improved catalytic performance compared to the conventional processes. The comparison of 3D-structured design with conventional batch and packed bed reactors serves as a reference to the state-of-the-art technology. The data presented show a clear advantage of the printed configuration of the channels and distribution of metals in it over conventional configurations (batch and packed bed) both in terms of alternative loading (FeCo on Al_2O_3) and stacking arrangement . It was shown that the alternative stacking of Fe on Al_2O_3 and FePd on GO can significantly improve the performance resulting in an increase of up to 90% in TOF in comparison to the FePd on GO batch analogue. The clear conclusion of this study is that the reactor concept and its configuration and operating conditions have led to optimised performance in terms of conversion, selectivity and TOF as successfully demonstrated in the case of FeCo@Al_2O_3 '1-3' monoliths. In contrast, its FePd@Al_2O_3 1-3 analogue exhibit a significantly lower selectivity toward Benzaldehyde as the secondary reaction proceeds from Benzaldehyde to benzoic acid. In addition, the mixed gas-liquid flow regime inside the microstructured reactor was successfully described with a dispersion model, as was determined from the residence time experiments. It was found that the concentration of oxygen in DMF is limiting and needs to be replenished by mass transfer from the gas to the liquid phase. A good agreement was found with the measured and simulated BA conversion and selectivity towards BZ after appropriate kinetic constants were obtained, for the FeCo@Al_2O_3 catalyst.

ABBREVIATIONS

BA - Benzyl Alcohol

BZ - Benzyl Aldehyde

DMF - N,N-Dimethylformamide

EDX – Energy-dispersive X-ray spectroscopy

HPLC - High Performance Liquid Chromatography

PGM - Platinium Groups Metals

RTD - Residence Time Distribution

SCCM - Standard Cubic Centimeters per Minute

SEM - Scanning Electron Microscopy

XRD - X-ray diffraction

REFERENCES

(1)   Galvanin, F.; Sankar, M.; Cattaneo, S.; Bethell, D.; Dua, V.; Hutchings, G. J.; Gavriilidis, A. On the Development of Kinetic Models for Solvent-Free Benzyl Alcohol Oxidation over a Gold-Palladium Catalyst. *Chem. Eng. J.* **2018**, *342*, 196–210. https://doi.org/10.1016/j.cej.2017.11.165.

(2)   Gemoets, H. P. L.; Su, Y.; Shang, M.; Hessel, V.; Luque, R.; Noël, T. Liquid Phase Oxidation Chemistry in Continuous-Flow Microreactors. *Chem. Soc. Rev.* **2015**, *45* (1), 83–117. https://doi.org/10.1039/C5CS00447K.

(3)   Vaccaro, L.; Lanari, D.; Marrocchi, A.; Strappaveccia, G. Flow Approaches towards Sustainability. *Green Chem.* **2014**, *16* (8), 3680–3704. https://doi.org/10.1039/C4GC00410H.

(4)   Wiles, C.; Watts, P. Continuous Flow Reactors: A Perspective. *Green Chem.* **2012**, *14* (1), 38–54. https://doi.org/10.1039/C1GC16022B.

(5)   Tojo, G.; Fernandez, M. I. *Oxidation of Alcohols to Aldehydes and Ketones: A Guide to Current Common Practice*; Springer Science & Business Media, 2006.

(6)   J.P., L.; I, H.; B, B.; F, F.; J.C, G.-O.; A, A. Process Network Synthesis for Benzaldehyde Production: P-Graph Approach. *Chem. Eng. Trans.* **2015**, 1369–1374. https://doi.org/10.3303/CET1545229.

(7)   Benzaldehyde Market Global Analysis, Worldwide Opportunities Industry Production, Size, Share, Drivers and Regional Outlook To 2022 https://www.marketwatch.com/press-release/benzaldehyde-market-global-analysis-worldwide-opportunities-industry-production-size-share-drivers-and-regional-outlook-to-2022-2019-03-18 (accessed 2019 -11 -29).

(8)   Miedziak, P. J.; He, Q.; Edwards, J. K.; Taylor, S. H.; Knight, D. W.; Tarbit, B.; Kiely, C. J.; Hutchings, G. J. Oxidation of Benzyl Alcohol Using Supported Gold–Palladium Nanoparticles. *Catal. Today* **2011**, *163* (1), 47–54. https://doi.org/10.1016/j.cattod.2010.02.051.

(9)   Miedziak, P.; Sankar, M.; Dimitratos, N.; Lopez-Sanchez, J. A.; Carley, A. F.; Knight, D. W.; Taylor, S. H.; Kiely, C. J.; Hutchings, G. J. Oxidation of Benzyl Alcohol Using Supported Gold–Palladium Nanoparticles. *Catal. Today* **2011**, *164* (1), 315–319. https://doi.org/10.1016/j.cattod.2010.10.028.

(10)   Meenakshisundaram, S.; Nowicka, E.; Miedziak, P. J.; Brett, G. L.; Jenkins, R. L.; Dimitratos, N.; Taylor, S. H.; Knight, D. W.; Bethell, D.; Hutchings, G. J. Oxidation of Alcohols Using Supported Gold and Gold–Palladium Nanoparticles. *Faraday Discuss.* **2010**, *145* (0), 341–356. https://doi.org/10.1039/B908172K.

(11)   Li, Y.; Sabbaghi, A.; Huang, J.; Li, K. C.; Tsui, L. S.; Lam, F. L. Y.; Hu, X. Aerobic Oxidation of Benzyl Alcohol: Influence from Catalyst Basicity, Acidity, and Preparation Methods. *Mol. Catal.* **2020**, *485*, 110789. https://doi.org/10.1016/j.mcat.2020.110789.

(12)   Dell'Anna, M. M.; Mali, M.; Mastrorilli, P.; Cotugno, P.; Monopoli, A. Oxidation of Benzyl Alcohols to Aldehydes and Ketones under Air in Water Using a Polymer Supported Palladium Catalyst. *J. Mol. Catal. Chem.* **2014**, *386*, 114–119. https://doi.org/10.1016/j.molcata.2014.02.001.

(13)   Al-Marri, A. H.; Khan, M.; Shaik, M. R.; Mohri, N.; Adil, S. F.; Kuniyil, M.; Alkhathlan, H. Z.; Al-Warthan, A.; Tremel, W.; Tahir, M. N.; Khan, M.; Siddiqui, M. R. H. Green Synthesis of Pd@graphene Nanocomposite: Catalyst for the Selective Oxidation of Alcohols. *Arab. J. Chem.* **2016**, *9* (6), 835–845. https://doi.org/10.1016/j.arabjc.2015.12.007.

(14)   Sun, J.; Tong, X.; Liu, Z.; Liao, S.; Zhuang, X.; Xue, S. Gold-Catalyzed Selectivity-Switchable Oxidation of Benzyl Alcohol in the Presence of Molecular Oxygen. *Catal. Commun.* **2016**, *85*, 70–74. https://doi.org/10.1016/j.catcom.2016.07.018.

(15)   Gómez-Villarraga, F.; Radnik, J.; Martin, A.; Köckritz, A. Synergistic Effect in the Oxidation of Benzyl Alcohol Using Citrate-Stabilized Gold Bimetallic Nanoparticles Supported on Alumina. *J. Nanoparticle Res.* **2016**, *18* (6). https://doi.org/10.1007/s11051-016-3453-7.

(16)   Çakır, V.; Saka, E. T.; Bıyıklıoğlu, Z.; Kantekin, H. Highly Selective Oxidation of Benzyl Alcohol Catalyzed by New Peripherally Tetra-Substituted Fe(II) and Co(II) Phthalocyanines. *Synth. Met.* **2014**, *197*, 233–239. https://doi.org/10.1016/j.synthmet.2014.09.022.

(17)   Al Badran, F.; Awdry, S.; Kolaczkowski, S. T. Development of a Continuous Flow Reactor for Pharmaceuticals Using Catalytic Monoliths: Pt/C Selective Oxidation of Benzyl Alcohol. *Catal. Today* **2013**, *216*, 229–239. https://doi.org/10.1016/j.cattod.2013.04.017.

(18)   Wu, G.; Cao, E.; Ellis, P.; Constantinou, A.; Kuhn, S.; Gavriilidis, A. Continuous Flow Aerobic Oxidation of Benzyl Alcohol on Ru/Al2O3 Catalyst in a Flat Membrane Microchannel Reactor: An Experimental and Modelling Study. *Chem. Eng. Sci.* **2019**, *201*, 386–396. https://doi.org/10.1016/j.ces.2019.02.015.

(19)   Bavykin, D. V.; Lapkin, A. A.; Kolaczkowski, S. T.; Plucinski, P. K. Selective Oxidation of Alcohols in a Continuous Multifunctional Reactor: Ruthenium Oxide Catalysed Oxidation of Benzyl Alcohol. *Appl. Catal. Gen.* **2005**, *288* (1), 175–184. https://doi.org/10.1016/j.apcata.2005.04.042.

(20)   Ratnam, A.; Kumari, S.; Kumar, R.; Singh, U. P.; Ghosh, K. Selective Oxidation of Benzyl Alcohol Catalyzed by Ruthenium (III) Complexes Derived from Tridentate Mer-Ligands Having Phenolato Donor. *J. Organomet. Chem.* **2020**, *905*, 120986. https://doi.org/10.1016/j.jorganchem.2019.120986.

(21)   Mao, D.; Qiu, J.; Jia, M.; Zhang, X.-F.; Yao, J. Platinum Supported Cellulose Based Carbon with Oxygen-Containing Functional Groups for Benzyl Alcohol Oxidation. *J. Phys. Chem. Solids* **2019**, *135*, 109095. https://doi.org/10.1016/j.jpcs.2019.109095.

(22)   Wilde, C. A.; Ryabenkova, Y.; Firth, I. M.; Pratt, L.; Railton, J.; Bravo-Sanchez, M.; Sano, N.; Cumpson, P. J.; Coates, P. D.; Liu, X.; Conte, M. Novel Rhodium on Carbon Catalysts for the Oxidation of Benzyl Alcohol to Benzaldehyde: A Study of the Modification of Metal/Support Interactions by Acid Pre-Treatments. *Appl. Catal. Gen.* **2019**, *570*, 271–282. https://doi.org/10.1016/j.apcata.2018.11.006.

(23)   Cruz, P.; Pérez, Y.; del Hierro, I.; Fajardo, M. Copper, Copper Oxide Nanoparticles and Copper Complexes Supported on Mesoporous SBA-15 as Catalysts in the Selective Oxidation of Benzyl Alcohol in Aqueous Phase. *Microporous Mesoporous Mater.* **2016**, *220*, 136–147. https://doi.org/10.1016/j.micromeso.2015.08.029.

(24)   Thao, N. T.; Nhu, N. T.; Lin, K.-S. Liquid Phase Oxidation of Benzyl Alcohol to Benzaldehyde over Sepiolite Loaded Chromium Oxide Catalysts. *J. Taiwan Inst. Chem. Eng.* **2018**, *83*, 10–22. https://doi.org/10.1016/j.jtice.2017.11.034.

(25)   Mallat, T.; Baiker, A. Oxidation of Alcohols with Molecular Oxygen on Solid Catalysts. *Chem. Rev.* **2004**, *104* (6), 3037–3058. https://doi.org/10.1021/cr0200116.

(26)   Zhan, B.-Z.; Thompson, A. Recent Developments in the Aerobic Oxidation of Alcohols. *Tetrahedron* **2004**, *60* (13), 2917–2935. https://doi.org/10.1016/j.tet.2004.01.043.

(27)   Galvanin, F.; Al-Rifai, N.; Cao, E.; Venkat, M.; Hutchings, G.; Gavriilidis, A.; Dua, V. Merging Information from Batch and Continuous Flow Experiments for the Identification of Kinetic Models of Benzyl Alcohol Oxidation over Au-Pd Catalyst. In *Computer Aided Chemical Engineering*; Kravanja, Z., Bogataj, M., Eds.; 26 European Symposium on Computer Aided Process Engineering; Elsevier, 2016; Vol. 38, pp 961–966. https://doi.org/10.1016/B978-0-444-63428-3.50165-X.

(28)   Zhou, X.; Liu, C. Three-Dimensional Printing for Catalytic Applications: Current Status and Perspectives. *Adv. Funct. Mater.* **2017**, *27* (30), 1701134. https://doi.org/10.1002/adfm.201701134.

(29)   Hurt, C.; Brandt, M.; Priya, S. S.; Bhatelia, T.; Patel, J.; Selvakannan, P.; Bhargava, S. Combining Additive Manufacturing and Catalysis: A Review. *Catal. Sci. Technol.* **2017**, *7* (16), 3421–3439. https://doi.org/10.1039/C7CY00615B.

(30)   Parra-Cabrera, C.; Achille, C.; Kuhn, S.; Ameloot, R. 3D Printing in Chemical Engineering and Catalytic Technology: Structured Catalysts, Mixers and Reactors. *Chem. Soc. Rev.* **2017**, *47*. https://doi.org/10.1039/C7CS00631D.

(31)   Middelkoop, V.; Slater, T.; Florea, M.; Neațu, F.; Danaci, S.; Onyenkeadi, V.; Boonen, K.; Saha, b; Baragau, I.-A.; Kellici, S. Next Frontiers in Cleaner Synthesis: 3D Printed Graphene-Supported CeZrLa Mixed-Oxide Nanocatalyst for CO2 Utilisation and Direct Propylene Carbonate Production. *J. Clean. Prod.* **2019**, *214*, 606–614. https://doi.org/Middelkoop, V., Slater, T., Florea, M., Neațu, F., Danaci, S., Onyenkeadi, V., Boonen, K., Saha, B., Baragau, I.A., and Kellici, S.   (2019).   Next frontiers in cleaner synthesis: 3D printed graphene-supported CeZrLa mixed-oxide nanocatalyst for CO2 utilisation and direct propylene carbonate production.   Journal of Cleaner Production,   214   606-614.   doi: https://doi.org/10.1016/j.jclepro.2018.12.274 <https://doi.org/10.1016/j.jclepro.2018.12.274>.

(32)   Díaz-Marta, A. S.; Tubío, C. R.; Carbajales, C.; Fernández, C.; Escalante, L.; Sotelo, E.; Guitián, F.; Barrio, V. L.; Gil, A.; Coelho, A. Three-Dimensional Printing in Catalysis: Combining 3D Heterogeneous Copper and Palladium Catalysts

for Multicatalytic Multicomponent Reactions. *ACS Catal.* **2018**, *8* (1), 392–404. https://doi.org/10.1021/acscatal.7b02592.

(33) Azuaje, J.; Tubío, C. R.; Escalante, L.; Gómez, M.; Guitián, F.; Coelho, A.; Caamaño, O.; Gil, A.; Sotelo, E. An Efficient and Recyclable 3D Printed α-Al2O3 Catalyst for the Multicomponent Assembly of Bioactive Heterocycles. *Appl. Catal. Gen.* **2017**, *C* (530), 203–210. https://doi.org/10.1016/j.apcata.2016.11.031.

(34) Tubío, C. R.; Azuaje, J.; Escalante, L.; Coelho, A.; Guitián, F.; Sotelo, E.; Gil, A. 3D Printing of a Heterogeneous Copper-Based Catalyst. *J. Catal.* **2016**, *C* (334), 110–115. https://doi.org/10.1016/j.jcat.2015.11.019.

(35) García, S.; Poulston, S.; Modeshia, D.; Stavarek, P.; Ujcic, M.; Lali, F.; Alves, M. A.; Araújo, J. D.; Krusche, M.; Ullrich, F.; Maier, D. Continuous Production of Squalane Using 3D Printed Catalytic Supports https://www.ingentaconnect.com/content/matthey/jmtr/2019/00000063/00000003/art00007;jsessionid=2qgofgd4cir3n.x-ic-live-01 (accessed 2020 -03 -02). https://doi.org/info:doi/10.1595/205651319X15535963555844.

(36) Pradhan, S. R.; Nair, V.; Giannakoudakis, D. A.; Lisovytskiy, D.; Colmenares, J. C. Design and Development of TiO2 Coated Microflow Reactor for Photocatalytic Partial Oxidation of Benzyl Alcohol. *Mol. Catal.* **2020**, *486*, 110884. https://doi.org/10.1016/j.mcat.2020.110884.

(37) Nair, V.; Colmenares, J. C.; Lisovytskiy, D. Ultrasound Assisted ZnO Coating in a Microflow Based Photoreactor for Selective Oxidation of Benzyl Alcohol to Benzaldehyde. *Green Chem.* **2019**, *21* (6), 1241–1246. https://doi.org/10.1039/C8GC03131B.

(39) Fakeeha, A. H.; Ibrahim, A. A.; Khan, W. U.; Seshan, K.; Al Otaibi, R. L.; Al-Fatesh, A. S. Hydrogen Production via Catalytic Methane Decomposition over Alumina Supported Iron Catalyst. *Arab. J. Chem.* **2018**, *11* (3), 405–414. https://doi.org/10.1016/j.arabjc.2016.06.012.

(40) Rahmati, M.; Huang, B.; Mortensen, M. K.; Keyvanloo, K.; Fletcher, T. H.; Woodfield, B. F.; Hecker, W. C.; Argyle, M. D. Effect of Different Alumina Supports on Performance of Cobalt Fischer-Tropsch Catalysts. *J. Catal.* **2018**, *359*, 92–100. https://doi.org/10.1016/j.jcat.2017.12.027.

(41) Vedyagin, A. A.; Volodin, A. M.; Kenzhin, R. M.; Stoyanovskii, V. O.; Rogov, V. A.; Kriventsov, V. V.; Mishakov, I. V. The Role of Chemisorbed Water in Formation and Stabilization of Active Sites on Pd/Alumina Oxidation Catalysts. *Catal. Today* **2018**, *307*, 102–110. https://doi.org/10.1016/j.cattod.2017.01.033.

(42) Spasiano, D.; Marotta, R.; Gargano, I.; Somma, I. D.; Vitiello, G.; D'Errico, G.; Andreozzi, R. Kinetic Modeling of Partial Oxidation of Benzyl Alcohol in Water by Means of Fe(III)/O2/UV–Solar Simulated Process. *Chem. Eng. J.* **2014**, *249*, 130–142. https://doi.org/10.1016/j.cej.2014.03.076.

(43) Di Somma, I.; Russo, D.; Andreozzi, R.; Marotta, R.; Guido, S. Kinetic Modelling of Benzyl Alcohol Selective Oxidation in Aqueous Mixtures of Nitric and Sulfuric Acids. *Chem. Eng. J.* **2017**, *308*, 738–744. https://doi.org/10.1016/j.cej.2016.09.113.

(44) Zhou, L.; Yu, D.; Wang, Z.; Cheng, L.-J.; Jin, Z.-H.; Weng, J.-J.; Yang, J.-Z.; Tian, Z.-Y. A Detailed Kinetic Study on Oxidation of Benzyl Alcohol. *Combust. Flame* **2019**, *207*, 10–19. https://doi.org/10.1016/j.combustflame.2019.05.034.

(45) Köckritz, A.; Sebek, M.; Dittmar, A.; Radnik, J.; Brückner, A.; Bentrup, U.; Pohl, M.-M.; Hugl, H.; Mägerlein, W. Ru-Catalyzed Oxidation of Primary Alcohols. *J. Mol. Catal. Chem.* **2006**, *246* (1–2), 85–99. https://doi.org/10.1016/j.molcata.2005.10.020.

(46) Venezia, B.; Douthwaite, M.; Wu, G.; Sankar, M.; Ellis, P.; Hutchings, G. J.; Gavriilidis, A. Slurry Loop Tubular Membrane Reactor for the Catalysed Aerobic Oxidation of Benzyl Alcohol. *Chem. Eng. J.* **2019**, *378*, 122250. https://doi.org/10.1016/j.cej.2019.122250.

(47) Sato, T.; Hamada, Y.; Sumikawa, M.; Araki, S.; Yamamoto, H. Solubility of Oxygen in Organic Solvents and Calculation of the Hansen Solubility Parameters of Oxygen. *Ind. Eng. Chem. Res.* **2014**, *53* (49), 19331–19337. https://doi.org/10.1021/ie502386t.